

pubs.acs.org/NanoLett Letter

# Impact of the Angular Alignment on the Crystal Field and Intrinsic Doping of Bilayer Graphene/BN Heterostructures

Liam S. Farrar, Gaia Maffione, Viet-Hung Nguyen, Kenji Watanabe, Takashi Taniguchi, Jean-Christophe Charlier, Dominique Mailly, and Rebeca Ribeiro-Palau\*

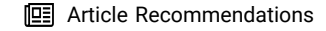


Cite This: Nano Lett. 2025, 25, 2236-2241



**ACCESS** I

III Metrics & More



SI Supporting Information

ABSTRACT: The ability to tune the energy gap in bilayer graphene makes it the perfect playground for the study of the effects of internal electric fields, such as the crystalline field, which are developed when other layered materials are deposited on top of it. Here, we introduce a novel device architecture allowing simultaneous control over the applied displacement field and the crystalline alignment between two materials. Our experimental and numerical results confirm that the crystal field and electrostatic doping due to the interface reflect the 120° symmetry of the bilayer graphene/BN heterostructure and are highly affected by the commensurate state. These results provide unique insight into the role of twist angle in the development of internal crystal fields and intrinsic electrostatic doping in heterostructures. Our results highlight the importance of layer alignment, beyond the existence

Flexible electrode

Metallic top gate

Intrinsic displacement field

Graphite bottom gate

highlight the importance of layer alignment, beyond the existence of a moiré superlattice, to understand the intrinsic properties of a heterostructure.

KEYWORDS: crystal field, heterostructures, graphene, angle control, intrinsic doping

V an der Waals heterostructures have become the perfect playground for condensed matter physics, especially since the angular alignment between layers was added as a new knob to tune their properties. Using the right combination of materials and twist angle, very complex phenomena can be observed in these heterostructures, such as superconductivity, 1-5 Mott insulators, 6 anomalous quantum Hall effect, 7 and more recently ferroelectricity.<sup>8-11</sup> However, mastering all of the parameters to have ultimate control of the properties of the heterostructure requires a deep understanding of the materials that compose the heterostructure and their interfaces. At these interfaces, crystal field effects result from the electrochemical difference between layers, modifying the properties of the heterostructure.<sup>12</sup> Measuring the effect of the crystal field in the heterostructure has only been addressed recently for fixed crystallographic alignments. 12 This is mostly because investigating the angular variations will require the integration of dynamically rotatable van der Waals heterostructures 13,14 with techniques that allow us to control both the top and bottom gates, which implies an important technological challenge.

In this work, we present a new device architecture that, in addition to the rotational control of van der Waals heterostructures, provides control over both the top and bottom electrostatic gates. We demonstrate the performance of this new architecture using Bernal-stacked bilayer graphene (BBG) stacked between hexagonal boron nitride (BN). The

control over both angular alignment and displacement field allows us to extract the angular dependence of the crystal electric field and intrinsic doping in a van der Waals heterostructure, pointing out the important role of layer alignment beyond the formation of moiré superlattices.

Figures 1a and b illustrate our novel device design, as both an overview (a) and its cross-section (b); Figure 1c shows atomic force microscope (AFM) images of a device in operation. The device comprises two main components: first, a Hall-bar shaped BBG on a BN layer, which itself sits atop a pre-etched graphite electrode, separated from the BBG by a BN layer; second, a rotator made of BN and Ti/Au, connected via an etched graphite electrode. The bottom graphite gate matches the rotator in diameter, and the graphite atop the rotator acts as a flexible van der Waals electrode for the application of a top gate voltage, <sup>15</sup> creating a dual-gated region centered on the BBG Hall bar. The Si substrate is highly doped in order to improve the contact resistances on the BBG far from the rotator by tuning the carrier density with a gate

Received: October 28, 2024 Revised: January 23, 2025 Accepted: January 27, 2025 Published: January 30, 2025





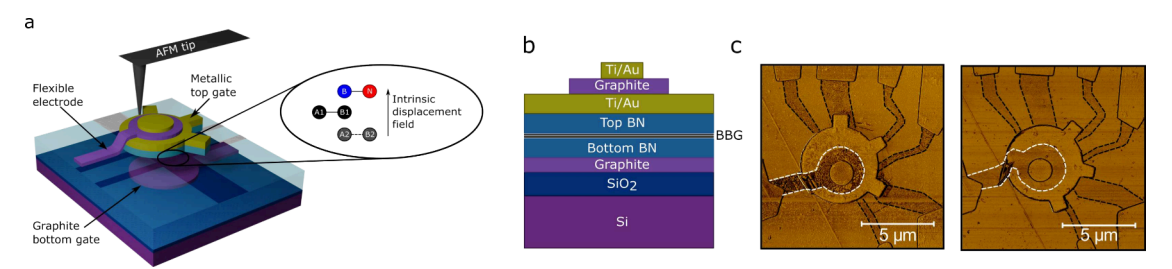


Figure 1. Dual gated rotatable device architecture. a and b, Illustration of the new device architecture (a) and its schematic cross-section (b). The zoom in (a) is meant to signal the BBG unit cell and the intrinsic displacement field. A1(2) and B1(2) represent carbon atoms in sublattice A and B of layer 1 (2), respectively. B (blue) and N (red) represent boron and nitrogen atoms, respectively. c, Atomic force microscopy images (phase signal) of a complete device before and after rotation. The graphite flexible electrode (white dashed line) and graphene Hall bar (black dashed lines) have been highlighted for clarity.

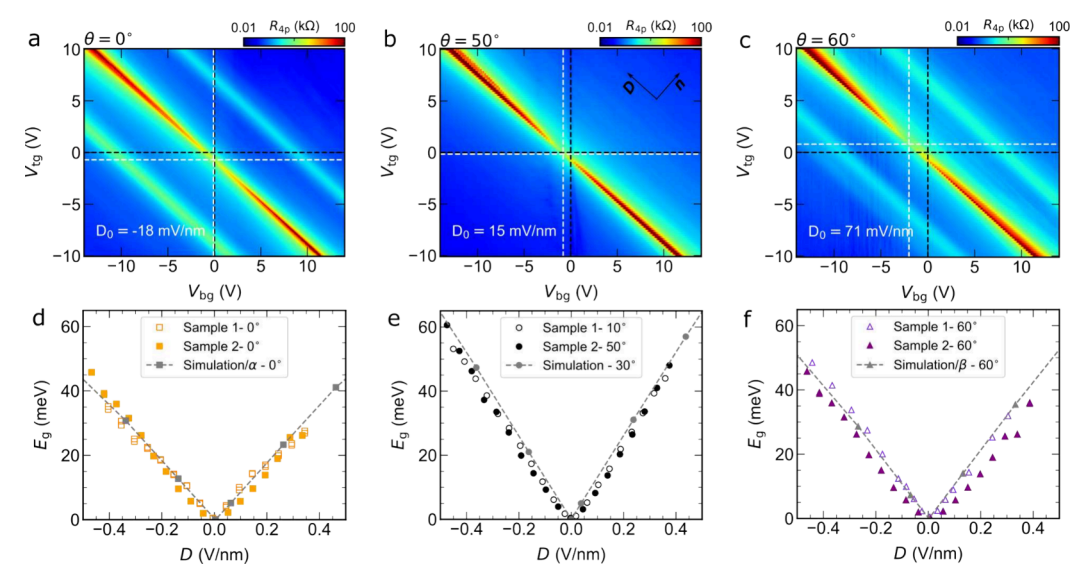


Figure 2. Dual gate effect at different rotational angles. Four-terminal resistance,  $R_{\rm 4P}$ , as a function of top  $(V_{\rm tg})$  and bottom  $(V_{\rm bg})$  gate voltages at  $\theta_{\rm top}=0^{\circ}$  (a),  $\theta_{\rm top}=50^{\circ}$  (b), and  $\theta_{\rm top}=60^{\circ}$  (c) of alignment between the top BN and the BBG for Sample 2 taken at T=10 K. Black dashed lines represent the  $V_{\rm tg}=0$  V and  $V_{\rm bg}=0$  V lines. White dashed lines show the position of the lowest value on resistance of the CNP. d–f, Energy gap,  $E_{\rm g}$ , as a function of the total displacement field, D, for three alignments:  $\theta_{\rm top}=0^{\circ}$  (d),  $\theta_{\rm top}=10^{\circ}/50^{\circ}$  (e), and  $\theta_{\rm top}=60^{\circ}$  (f), for Sample 1 and Sample 2. The data points are extracted from the Arrhenius plot in the thermally activated regime. Gray points with dashed lines are the result of numerical simulations divided by a factor  $\alpha=1.4$  and  $\beta=1.2$  for 0° and 60°, respectively. See main text.

voltage.<sup>16</sup> Full details of the fabrication procedures as well as optical images of the devices are provided in Supporting Information Note 1. It is important to mention that the bottom BN and graphene are intentionally misaligned via straight edge identification.

The rotation procedure is identical with our previous reports, 13,17 wherein an AFM tip is used to mechanically push the rotator while measuring simultaneously the resistance of the sample, thus providing in situ control of the crystallographic alignment between the top BN and the BBG underneath. Overall, the device allowed for rotational control within 140°. In the AFM images of Figure 1c we can see examples where the BN handle is rotated by about 37° after being pushed with the AFM tip. In this report, we present results obtained mainly in three samples: Sample 1 and Sample 2, which share the same bottom BN, and Sample 3 (see Supporting Information Note 2). The Hall bar widths w and lengths l are  $w = l = 1.5 \mu m$ . The carrier mobility of our samples ranged from 100,000 to 200,000 cm<sup>2</sup> V<sup>-1</sup> s<sup>-1</sup> for intermediate densities  $\pm 0.65 \times 10^{12}$  cm<sup>2</sup> at T < 40 K. The mean free path was calculated to be  $\approx 1.5 \mu m$  for the same

carrier density below T < 40 K, reflecting the ballistic character of the charge transport for all of our devices.

To demonstrate the efficiency of our dual gated rotatable devices, we show in Figures 2a–c measurements of the four-probe resistance of sample 2 at 10 K as a function of  $V_{\rm bg}$  and  $V_{\rm tg}$  at three different angles:  $\theta_{\rm top}=0^{\circ}$  (a),  $\theta_{\rm top}\approx 50^{\circ}$  (b), where the moiré has little to no influence, and  $\theta_{\rm top}=60^{\circ}$  (c).

In BBG, when the signs of  $V_{\rm bg}$  and  $V_{\rm tg}^{'}$  are opposite we observe a rapidly increasing  $R_{\rm 4P}$  at the charge neutrality point (CNP). This maximum resistance for the three alignments traces a straight line, with a slope determined by the ratio of the capacitive coupling of each layer  $C_{\rm tg}/C_{\rm bg}$ , which is in turn directly related to the thickness ratio between the top and bottom BN layers. Along this diagonal line, the resistance strongly increases, a clear sign that a band energy gap is opening, as the magnitude of the displacement field |D| increases. The total displacement field, D, and total carrier density,  $n_{\rm T}$ , of the system can be expressed as

$$D = D_{A} - D_{0} = \frac{e}{2\epsilon_{0}} [C_{tg}V_{tg} - C_{bg}V_{bg}] - D_{0}$$
(1)

and

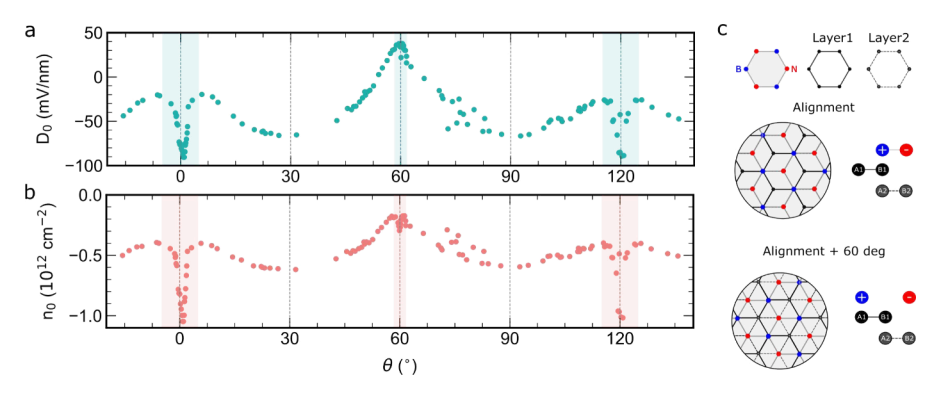


Figure 3. Crystal field and intrinsic doping as a function of angle. a, Angular dependence of the internal displacement field generated by the presence of the top and bottom BN. b, Angular dependence of the intrinsic doping of the system. Shadow areas around  $0^{\circ}$ ,  $60^{\circ}$ , and  $120^{\circ}$  represent the  $\pm 5^{\circ}$  ( $\pm 2^{\circ}$ ) segment where a deviation from the expected behavior is observed for  $0^{\circ}$  ( $60^{\circ}$ ). Measurements taken for sample 3. c, Schematic representation of the two crystallographic alignments separated by  $60^{\circ}$ . Here positive charge accumulation on B (blue) atoms and negative charge accumulation on N (red) atoms is represented by (+) and (-) signs, respectively.

$$n_{\rm T} = n - n_0 = [C_{\rm tg}V_{\rm tg} + C_{\rm bg}V_{\rm bg}] - n_0$$
 (2)

where  $D_{\rm A}$  is the applied displacement field;  $D_0$  is the residual or intrinsic displacement field of the sample;  $n_0$  is the residual carrier density or intrinsic doping of the bilayer;  $C_{\rm b(t)g} = \epsilon_0 \epsilon / d_{\rm b(t)} e$  is the bottom (top) gate capacitive coupling, directly extracted from the Hall effect;  $\epsilon$  is the BN dielectric constant;  $d_{\rm b(t)}$  is the BN thickness of the bottom (top) gate; and  $\epsilon_0$  is the vacuum permittivity.

The behaviors of the two aligned positions  $\theta_{\rm top}=0^{\circ}$  and  $\theta_{\rm top}=60^{\circ}$ , Figure 2a and c, are dissimilar due to the  $120^{\circ}$  symmetry of the BN/BBG heterostructure  $^{17}$  and are distinguished by the relative heights of the room temperature four-probe resistance measurements (see Supporting Information Note 3 for further details). At low temperatures, their alignment is indicated by the presence of satellite peaks which appear symmetrically in carrier density around the CNP and occur due to the emergence of satellite Dirac points induced by scattering from the moiré superlattice potential. The moiré wavelength  $\lambda$  is accurately determined by magneto-transport measurements and corresponds to  $\lambda = 14.2 \pm 0.1$  nm and  $\lambda = 14.0 \pm 0.1$  nm for the  $0^{\circ}$  and  $60^{\circ}$  alignments, respectively (see Supporting Information, Note 4 for further details).

Notice that for the aligned positions, contrary to the CNP, the resistance of the satellite peaks does not significantly change with displacement field (Figure 2a and c). This means that these peaks are not affected by the breaking of inversion symmetry created by the displacement field.

To determine the residual or intrinsic displacement field,  $D_0$ , we followed the resistance at the CNP as a function of both electrostatic gates. As explained before, the CNP can be clearly seen as the red diagonal line in Figure 2a-c, which indicates a strong resistance. The lowest resistance value along this diagonal line is the point where applied  $V_{\rm bg}$  and  $V_{\rm tg}$  fully close the energy band gap. We marked it by the crossing of white dashed lines in Figure 2a-c. At this point the applied displacement field,  $D_{\rm A}$ , compensates the intrinsic displacement field,  $D_{\rm O}$ , of the sample. The origin of the intrinsic displacement field, as well as the residual doping, in single gated devices has been attributed to contaminants and residues on the surface of the device; however, it is more difficult to spot its origin in the case of double gated devices, as in our cases; see discussion below.

The energy gap,  $E_g$ , induced by the applied displacement field can be determined by the temperature dependence of the

CNP resistance. In the thermally activated regime, the resistance at the CNP decays exponentially as  $R_{\rm CNP}$   $\propto$  $\exp(E_{\rm g}/(2k_{\rm BT}))$ , where  $k_{\rm B}$  is the Boltzmann's constant and T the temperature (Supporting Information, Note 5). In Figure 2d-f we plot the dependence of the energy gap on the total displacement field, D. All the curves follow an approximately linear dependence of the energy gap, as previously reported. 18,20,22 However, they do not have the same slope, depending on the angular alignment. For the misaligned cases (Figure 2e), the linear behavior is highly symmetric with respect to positive and negative displacement field, in agreement with previous reports.<sup>20</sup> On the other hand, for the aligned position (Figure 2d and f) the energy gap is slightly smaller. It is important to notice that, contrary to previous reports<sup>22</sup> and consistent with our earlier results, <sup>17</sup> we do not observe any thermal activated behavior for the satellite peaks at any value of the displacement field.

Let us discuss these features. The energy band gap,  $E_{\rm g}$  is given by  $^{23,24}$ 

$$E_{\rm g} = \frac{|\Delta|}{\sqrt{1 + (\Delta/\gamma_{\rm l})^2}} \tag{3}$$

where  $\gamma_1$  is the interlayer coupling strength between the graphene layers and  $\Delta$  is the onsite potential difference expressed as  $^{24,25}$ 

$$\Delta = \frac{d_0 e \tilde{D}}{\varepsilon_0 \varepsilon_z} + \frac{d_0 e^2}{2\varepsilon_0 \overline{\varepsilon}} \delta n(\Delta) \tag{4}$$

The first term of eq 4 results from the external (applied or intrinsic) displacement field, where  $\tilde{D}/\epsilon_0=D$  is the total displacement field;  $d_0$  is the interlayer spacing between the graphene layers; e is the elementary charge; and  $\varepsilon_z$ ,  $\overline{\varepsilon}$  are effective dielectric constants which vary depending on the model used. <sup>26,27</sup> In our numerical simulation we use  $\varepsilon_z=2.5.^{26}$  The second term of eq 4 results from the difference between the charge carrier densities in the upper  $n_1$  and lower  $n_2$  layers  $\delta n=n_2-n_1.$   $\delta n$  itself depends also on the value of  $\Delta$  and as such requires a self-consistent solution which, for the misaligned case, is presented elsewhere.

Intuitively, the difference observed for the energy gap between the aligned and misaligned cases could be explained as an effect of the commensurate state near crystallographic alignment, a local enlargement of the graphene lattice constant due to its van der Waals interaction with BN. <sup>17,28</sup> However, we have performed numerical simulations (same numerical methods as in ref 17), and the effects of the commensurate state in the energy gap seems only to be relevant at larger displacement field (see Supporting Information, Note 6).

By directly comparing the result of our numerical simulations with the experimental results of the energy gap as a function of displacement field, Figure 2d–f, we remark that the data from numerical simulations, for both aligned positions 0° and 60°, differ by a factor of  $\alpha=1.4$  and  $\beta=1.2$ . The origin of this discrepancy might come from the second term of eq 4 since the  $\delta n(\Delta)$  parameter is not included in our numerical simulation given the complexity of its implementation in a large moiré cell. This term seems to be negligible at the misaligned position since our numerical simulations fit very well the experimental data.

We can extract experimentally the angular dependence of  $\delta n_0$ , the difference between the charge carrier densities in the upper and lower layers without any applied displacement field (Figure 3a) by calculating the intrinsic displacement field. For this, we performed resistance measurements around the CNP, by varing  $V_{
m bg}$ , for fixed values of  $V_{
m tg}$  to obtain the values of  $V_{
m tg}$ and  $V_{\rm bg}$  for which the height of the CNP is the lowest, reflecting the closing of the energy gap (for details, see Supporting Information, Note 7). These experiments are performed at room temperature to achieve a high angular resolution, with several points confirmed at low temperature to ensure the reported phenomena remain stable across temperatures (for details, see Supporting Information, Note Note 7). Figure 3a shows the angular dependence of the intrinsic displacement field,  $D_0$ , which can be understood as the crystal field generated by the atomic configuration of the upper and bottom BN layers on the graphene layer. In these measurements, we observe a strong change at 0° occurring in a range of  $\pm 5^{\circ}$  and a change in the opposite direction for  $60^{\circ}$  of alignment that saturates for a range of angle of  $\pm 2^{\circ}$ . This indicates that the alignment of the BN layer to the graphene plays a major role since in the commensurate state strong local strains in graphene are induced by its interactions with BN affecting therefore the intrinsic displacement field.

The measurements described above also allow us to extract the angular dependence of intrinsic doping,  $n_0$ . In Figure 3b we can see that the intrinsic density, for misaligned angles, varies slowly with the angular alignment until it reaches the aligned positions. At these aligned positions,  $0^{\circ}$  and  $60^{\circ}$ , the behavior is opposite, increasing for  $0^{\circ}$  and decreasing for  $60^{\circ}$ , and this change is much more pronounced in the case of  $0^{\circ}$ . The physical origin of this particular dependence of the intrinsic doping with the angular alignment is difficult to elucidate. However, since it is much more pronounced at the aligned positions its origin can be intuitively assigned to the strain generated by the commensurate state. <sup>17</sup>

In order to understand this nontrivial dependence, we can start by comparing our experimental results with numerical simulations. As in the experiment, for the numerical simulations we have extracted the displacement field needed in order to close the energy gap of the electronic band structure for each angular alignment; from here on we will refer to this as the crystal field since it is a natural electric field generated by the atomic configuration of our system.

To determine the mentioned crystal field, we first calculate the energy gap of the system for a given angular alignment without applied displacement field, and then we numerically apply a displacement field in an opposite direction, i.e., in order to cancel the potential difference of graphene layers and therefore close the energy gap. In our simulations, the applied displacement field is simply computed by adjusting the onsite energies of each graphene layer, i.e.,  $\epsilon_{\text{Carbon}} = \pm \Delta/2$ , in the Hamiltonian of ref 17.

We can start by discussing the unrelaxed case, Figure 4a, for which we can see that the crystal field is minimum at 30° and

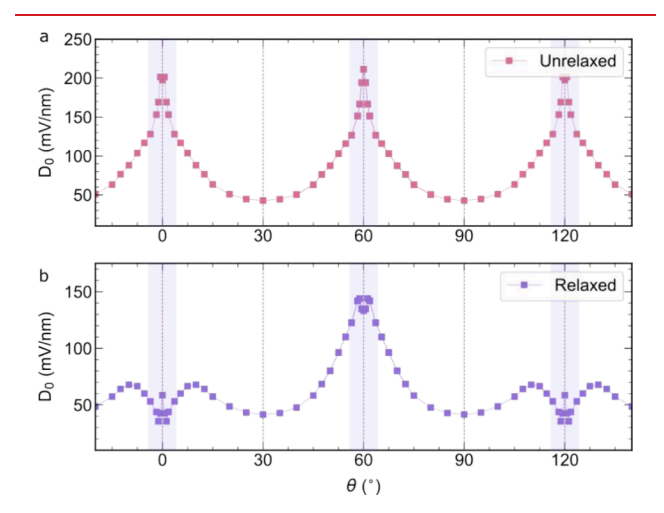


**Figure 4.** Crystal field numerical simulation. Intrinsic displacement field as a function of the angular alignment between bilayer graphene and a BN layer for a system without atomic relaxation (a) and one with atomic relaxation (b).

90° and increases strongly close to the aligned positions, i.e., 0°, 60°, and 120°. Note that the minimum value of the displacement field is not zero because we simulated a system with only one BN layer on top of the bilayer graphene. The strong increase of the crystal field at the aligned position is due to the combination of two factors: i) the electric field generated by the boron and nitrogen atoms by their proximity to the atoms A1 and B2 of the BBG (crystal field effect) (see Figure 3c), and ii) the moiré superlattice, which modifies the electronic band structure, even in the unrelaxed case. By using the numerical methods explained in ref 17 we relax the atomic structure (Figure 4b). This atomic relaxation will give rise to the stretching of the graphene lattice inside the moiré cell and the formation of wrinkles of unstretched graphene around these cells.

For the relaxed numerical simulations near crystallographic alignment the crystal field is highly impacted by the moiré superlattice, as predicted in ref 29. However, we can see that the impact for 0° and 60° has opposite behavior, which can be explained by looking at the unit cell of BBG for both aligned positions 0° and 60° (Figure 3c). In the commensurate state, at the inner part of the moiré cell the BBG atoms are arranged in a BA stacking, between the top layer of graphene and the BN layer. Here boron atoms are preferentially sitting on the carbon atoms since this is the most energetically favorable configuration. We have demonstrated in our previous report 17 that the difference in the stacking for both alignments gives rise to differences in the in-plane atomic displacement and therefore to the electronic transport characteristics.

In the case of the crystal field, the difference between boron (+) and nitrogen (-) will generate a different charge accumulation between sites A1 and B2, inducing a different

Nano Letters pubs.acs.org/NanoLett Letter

crystal field. This crystal field is expected to be stronger in one of the aligned cases because of the configuration of nitrogen and boron atoms, which also creates a larger  $\delta n_0$ . As this is observed within the same sample, we can disregard any effect of spurious doping, providing further evidence of the nonidentical nature of the two moiré in BBG/BN. It is important to note that our numerical simulations do not consider the bottom BN which induces an offset in Figure 3a, explaining the asymmetry with respect to zero crystal field. This can be seen in the Supporting Information, Note 7, where the general behavior of the curve for a different sample is the same as the curve is offset.

To conclude, we have developed a new device architecture that enables the rotation control of a van der Waals heterostructure, while allowing for simultaneous control of both bottom and top gates. We have used this device to reveal further details about the effects of the moiré superlattice such as its impact on the evolution of the band gap by an external displacement field. We have measured for the first time the evolution of the atomic crystal field with angular alignment in a van der Waals heterostructure and revealed the strong effects of the commensurate state. The commensurate state in aligned bilayer graphene/BN structures is, as predicted by our numerical simulations, 120° periodic. These results highlight the importance of minding the layer alignment of each layer, beyond the existence of a moiré superlattice, to understand and simulate the intrinsic properties of a van der Waals heterostructure.

#### ASSOCIATED CONTENT

### Supporting Information

The Supporting Information is available free of charge at https://pubs.acs.org/doi/10.1021/acs.nanolett.4c05378.

Additional experimental details, materials, methods, and theoretical model (PDF)

## AUTHOR INFORMATION

### **Corresponding Author**

Rebeca Ribeiro-Palau — Université Paris-Saclay, CNRS, Centre de Nanosciences et de Nanotechnologies (C2N), 91120 Palaiseau, France; orcid.org/0000-0001-6169-3128; Phone: +33 (0)1 70 27 06 92; Email: rebeca.ribeiro-palau@cnrs.fr

#### **Authors**

Liam S. Farrar – Université Paris-Saclay, CNRS, Centre de Nanosciences et de Nanotechnologies (C2N), 91120 Palaiseau, France

Gaia Maffione – Université Paris-Saclay, CNRS, Centre de Nanosciences et de Nanotechnologies (C2N), 91120 Palaiseau, France

Viet-Hung Nguyen – Institute of Condensed Matter and Nanosciences, Université Catholique de Louvain (UCLouvain), 1348 Louvain-la-Neuve, Belgium; orcid.org/0000-0001-6729-3520

Kenji Watanabe — Research Center for Electronic and Optical Materials, National Institute for Materials Science, Tsukuba 305-0044, Japan; orcid.org/0000-0003-3701-8119

Takashi Taniguchi — Research Center for Materials Nanoarchitectonics, National Institute for Materials Science, Tsukuba 305-0044, Japan; orcid.org/0000-0002-1467-3105 Jean-Christophe Charlier – Institute of Condensed Matter and Nanosciences, Université Catholique de Louvain (UCLouvain), 1348 Louvain-la-Neuve, Belgium

Dominique Mailly – Université Paris-Saclay, CNRS, Centre de Nanosciences et de Nanotechnologies (C2N), 91120 Palaiseau, France

Complete contact information is available at: https://pubs.acs.org/10.1021/acs.nanolett.4c05378

#### **Author Contributions**

\*L.S.F., G.M., and V.-H.N. contributed equally to this work.

Notes

The authors declare no competing financial interest.

#### ACKNOWLEDGMENTS

The authors acknowledge discussions with Hervé Aubin, Ulf Gennser, Nicolas Leconte, and Cory Dean. This work was done within the C2N micro nanotechnologies platforms and partly supported by the RENATECH network and the General Council of Essonne. This work was supported by ERC starting grant  $N^{\circ}$  853282 - TWISTRONICS (R.R.-P.), the DIM-SIRTEQ project TOPO2D, and the DIM QuanTIP project Q-MAG and IQUPS. R.R.-P. and J.-C.C. also acknowledge the Flag-Era JTC project TATTOOS (N° R.8010.19) and the Pathfinder project "FLATS" N° 101099139. V.H.N. and J.-C.C. also acknowledge fundings from the Fédération Wallonie-Bruxelles through the ARC project "DREAMS" ( $N^{\circ}$  21/26-116), from the EOS project "CONNECT" ( $N^{\circ}$  40007563), and from the Belgium F.R.S.-FNRS through the research project ( $N^{\circ}$  T.029.22F). Computational resources were provided by the CISM supercomputing facilities of UCLouvain and the CECI consortium funded by F.R.S.-FNRS of Belgium  $(N^{\circ} 2.5020.11)$ . K.W. and T.T. acknowledge support from the JSPS KAKENHI (Grant Numbers 21H05233 and 23H02052) and World Premier International Research Center Initiative (WPI), MEXT, Japan.

# ■ REFERENCES

- (1) Cao, Y.; Fatemi, V.; Fang, S.; Watanabe, K.; Taniguchi, T.; Kaxiras, E.; Jarillo-Herrero, P. Unconventional superconductivity in magic-angle graphene superlattices. *Nature* **2018**, *556*, 43–50.
- (2) Kim, H.; Choi, Y.; Lewandowski, C.; Thomson, A.; Zhang, Y.; Polski, R.; Watanabe, K.; Taniguchi, T.; Alicea, J.; Nadj-Perge, S. Evidence for unconventional superconductivity in twisted trilayer graphene. *Nature* **2022**, *606*, 494–500.
- (3) Yankowitz, M.; Chen, S.; Polshyn, H.; Zhang, Y.; Watanabe, K.; Taniguchi, T.; Graf, D.; Young, A. F.; Dean, C. R. Tuning superconductivity in twisted bilayer graphene. *Science* **2019**, *363*, 1059–1064.
- (4) Guo, Y.; Pack, J.; Swann, J.; Holtzman, L.; Cothrine, M.; Watanabe, K.; Taniguchi, T.; Mandrus, D. G.; Barmak, K.; Hone, J.; Millis, A. J.; Pasupathy, A.; Dean, C. R. Superconductivity in 5.0° twisted bilayer WSe2. *Nature* **2025**, *637*, 839–845.
- (5) Xia, Y.; Han, Z.; Watanabe, K.; Taniguchi, T.; Shan, J.; Mak, K. F. Superconductivity in twisted bilayer WSe2. *Nature* **2025**, *637*, 833–838.
- (6) Chen, G.; Jiang, L.; Wu, S.; Lyu, B.; Li, H.; Chittari, B. L.; Watanabe, K.; Taniguchi, T.; Shi, Z.; Jung, J.; Zhang, Y.; Wang, F. Evidence of a gate-tunable Mott insulator in a trilayer graphene moiré superlattice. *Nat. Phys.* **2019**, *15*, 237–241.
- (7) Serlin, M.; Tschirhart, C. L.; Polshyn, H.; Zhang, Y.; Zhu, J.; Watanabe, K.; Taniguchi, T.; Balents, L.; Young, A. F. Intrinsic quantized anomalous Hall effect in a moiré heterostructure. *Science* **2020**, *367*, 900–903.

Nano Letters pubs.acs.org/NanoLett Letter

- (8) Zheng, Z.; Ma, Q.; Bi, Z.; de La Barrera, S.; Liu, M.-H.; Mao, N.; Zhang, Y.; Kiper, N.; Watanabe, K.; Taniguchi, T.; et al. others Unconventional ferroelectricity in moiré heterostructures. *Nature* **2020**, 588, 71–76.
- (9) Niu, R.; Li, Z.; Han, X.; Qu, Z.; Ding, D.; Wang, Z.; Liu, Q.; Liu, T.; Han, C.; Watanabe, K.; et al. Giant ferroelectric polarization in a bilayer graphene heterostructure. *Nat. Commun.* **2022**, *13*, 6241.
- (10) Klein, D. R.; Xia, L.-Q.; MacNeill, D.; Watanabe, K.; Taniguchi, T.; Jarillo-Herrero, P. Electrical switching of a bistable moiré superconductor. *Nature Nanotechnol.* **2023**, *18*, 331–335.
- (11) Yan, X.; Zheng, Z.; Sangwan, V. K.; Qian, J. H.; Wang, X.; Liu, S. E.; Watanabe, K.; Taniguchi, T.; Xu, S.-Y.; Jarillo-Herrero, P.; et al. Moiré synaptic transistor with room-temperature neuromorphic functionality. *Nature* **2023**, *624*, 551–556.
- (12) Rickhaus, P.; Zheng, G.; Lado, J. L.; Lee, Y.; Kurzmann, A.; Eich, M.; Pisoni, R.; Tong, C.; Garreis, R.; Gold, C.; Masseroni, M.; Taniguchi, T.; Wantanabe, K.; Ihn, T.; Ensslin, K. Gap Opening in Twisted Double Bilayer Graphene by Crystal Fields. *Nano Lett.* **2019**, 19, 8821–8828.
- (13) Ribeiro-Palau, R.; Zhang, C.; Watanabe, K.; Taniguchi, T.; Hone, J.; Dean, C. R. Twistable electronics with dynamically rotatable heterostructures. *Science* **2018**, *361*, 690–693.
- (14) Inbar, A.; Birkbeck, J.; Xiao, J.; Taniguchi, T.; Watanabe, K.; Yan, B.; Oreg, Y.; Stern, A.; Berg, E.; Ilani, S. The quantum twisting microscope. *Nature* **2023**, *614*, 682–687.
- (15) Telford, E. J.; Benyamini, A.; Rhodes, D.; Wang, D.; Jung, Y.; Zangiabadi, A.; Watanabe, K.; Taniguchi, T.; Jia, S.; Barmak, K.; et al. Via method for lithography free contact and preservation of 2D materials. *Nano Lett.* **2018**, *18*, 1416–1420.
- (16) Ribeiro-Palau, R.; Chen, S.; Zeng, Y.; Watanabe, K.; Taniguchi, T.; Hone, J.; Dean, C. R. High-quality electrostatically defined Hall bars in monolayer graphene. *Nano Lett.* **2019**, *19*, 2583–2587.
- (17) Arrighi, E.; Nguyen, V.-H.; Di Luca, M.; Maffione, G.; Hong, Y.; Farrar, L.; Watanabe, K.; Taniguchi, T.; Mailly, D.; Charlier, J.-C.; et al. Non-identical moiré twins in bilayer graphene. *Nat. Commun.* **2023**, *14*, 8178.
- (18) Taychatanapat, T.; Jarillo-Herrero, P. Electronic transport in dual-gated bilayer graphene at large displacement fields. *Physical review letters* **2010**, *105*, 166601.
- (19) Zhang, Y.; Tang, T.-T.; Girit, C.; Hao, Z.; Martin, M. C.; Zettl, A.; Crommie, M. F.; Shen, Y. R.; Wang, F. Direct observation of a widely tunable bandgap in bilayer graphene. *Nature* **2009**, *459*, 820–823.
- (20) Icking, E.; Banszerus, L.; Wörtche, F.; Volmer, F.; Schmidt, P.; Steiner, C.; Engels, S.; Hesselmann, J.; Goldsche, M.; Watanabe, K.; et al. Transport spectroscopy of ultraclean tunable band gaps in bilayer graphene. *Adv. Electron. Mater.* **2022**, *8*, 2200510.
- (21) Yankowitz, M.; Xue, J.; Cormode, D.; Sanchez-Yamagishi, J. D.; Watanabe, K.; Taniguchi, T.; Jarillo-Herrero, P.; Jacquod, P.; LeRoy, B. J. Emergence of superlattice Dirac points in graphene on hexagonal boron nitride. *Nat. Phys.* **2012**, *8*, 382–386.
- (22) Iwasaki, T.; Morita, Y.; Watanabe, K.; Taniguchi, T. Dual-gated hBN/bilayer-graphene superlattices and the transitions between the insulating phases at the charge neutrality point. *Phys. Rev. B* **2022**, *106*, 165134.
- (23) Min, H.; Sahu, B.; Banerjee, S. K.; MacDonald, A. Ab initio theory of gate induced gaps in graphene bilayers. *Phys. Rev. B* **2007**, 75, 155115.
- (24) McCann, E. Asymmetry gap in the electronic band structure of bilayer graphene. *Phys. Rev. B* **2006**, *74*, 161403.
- (25) Jung, J.; MacDonald, A. H. Accurate tight-binding models for the  $\pi$  bands of bilayer graphene. *Phys. Rev. B* **2014**, *89*, 035405.
- (26) Slizovskiy, S.; Garcia-Ruiz, A.; Berdyugin, A. I.; Xin, N.; Taniguchi, T.; Watanabe, K.; Geim, A. K.; Drummond, N. D.; Fal'ko, V. I. Out-of-Plane Dielectric Susceptibility of Graphene in Twistronic and Bernal Bilayers. *Nano Lett.* **2021**, *21*, 6678–6683.
- (27) McCann, E.; Koshino, M. The electronic properties of bilayer graphene. Rep. Prog. Phys. 2013, 76, 056503.

- (28) Woods, C.; Britnell, L.; Eckmann, A.; Ma, R.; Lu, J.; Guo, H.; Lin, X.; Yu, G.; Cao, Y.; Gorbachev, R. V.; et al. Commensurate—incommensurate transition in graphene on hexagonal boron nitride. *Nat. Phys.* **2014**, *10*, 451–456.
- (29) Tepliakov, N. V.; Wu, Q.; Yazyev, O. V. Crystal Field Effect and Electric Field Screening in Multilayer Graphene with and without Twist. *Nano Lett.* **2021**, *21*, 4636–4642.
- (30) Jung, J.; DaSilva, A. M.; MacDonald, A. H.; Adam, S. Origin of band gaps in graphene on hexagonal boron nitride. *Nat. Commun.* **2015**, *6*, 1–11.